1   **REVISION 2**

2   **Nucleation Rates of Spherulites in Natural Rhyolitic Lava**

3

4

5   James E. Gardner[1,*], Kenneth S. Befus[2], James M. Watkins[3], and Travis Clow[1]

6

7

8

9   [1]Department of Geological Sciences, Jackson School of Geosciences,

10   The University of Texas at Austin, Austin, TX, 78712-0254, U.S.A.

11   [2]Department of Geosciences, Baylor University, Waco, TX, 76798, U.S.A.

12   [3]Department of Geological Sciences, University of Oregon,

13   Eugene, OR, 97403-1272, U.S.A.

14

15

16

17

18   [*]Author to whom correspondence should be addressed

19   (fax: 1-512-471-9425; office: 1-512-471-0953

20   e-mail: gardner@mail.utexas.edu)

21

22   **ABSTRACT**

23   The rates of nucleation and crystal growth from silicate melt are difficult to measure

24   because the temperature–time path of magma is often unknown. We use geochemical

25   gradients around spherulites in obsidian glass to estimate the temperature–time interval of

26   spherulite crystallization. This information is used in conjunction with new high-

27   resolution X-ray Computed Tomography (HRXCT) data on the size distributions of

28   spherulites in six samples of rhyolite obsidian lava to infer spherulite nucleation rates. A

29   large dataset of geochemical profiles indicate that the lavas cooled at rates of $10^{-2.2}$ to $10^{-1.2}$ °C hr^{-1}, and that the spherulites grew at rates that decreased exponentially with time,

31   with values of $10^{-0.70}$ to $10^{0.30}$ μm hr^{-1} at 600°C. Spherulites are estimated to have begun

32   nucleating when undercooling [ΔT, = liquidus T (≈800°C) minus nucleation T] reached

33   100–277°C, and stopped when ΔT = 203–365°C, with exact values dependent on

34   assumed cooling and growth rates. Regardless of rates, we find that spherulites nucleated

35   within a ~88–113°C temperature interval, and hence began when $\Delta T \approx 0.65$–$0.88 \times T_L$,

36   and peaked when $\Delta T \approx 0.59$–$0.80 \times T_L$. A peak rate of nucleation of 0.072±0.049 cm^{-3}

37   hr^{-1} occurred at 533±14°C, using cooling and growth rates that best fit the dataset of

38   geochemical profiles. While our inferred values for ΔT overlap those from experimental

39   studies, our nucleation rates are much lower. That difference likely results from

40   experimental studies using hydrous melts; the natural spherulites grew in nearly

41   anhydrous glass.

42

43   Keywords: spherulite, nucleation rate, growth rate, cooling rate, Yellowstone, obsidian

44

INTRODUCTION

45

46   Crystallization of molten magma affects magma rheology, volatile exsolution, and

47 has long been thought to be a dominant process in generating the vast array of magma

48 compositions seen on Earth (e.g., Bowen 1919, 1947; McKenzie 1984). Despite the

49 importance of crystallization to many problems in igneous petrology and volcanology,

50 the kinetics of crystallization, and hence the rate at which magma undergoes physical and

51 chemical changes, are not well understood. Much of our knowledge on crystallization

52 comes from laboratory experiments, where temperature and cooling rate are controlled.

53 There are, however, limits to laboratory investigations. For one, it is not yet possible to

54 observe the onset of crystallization because nucleation clusters consist of only 10's to

55 1000's of atoms (Lasaga, 1998). It is also difficult to measure the kinetics of

56 crystallization in highly viscous melts because of the long run times needed to achieve

57 visible crystals (e.g., Schairer and Bowen 1956; Johannes 1979). Experiments on crystal

58 nucleation in viscous melts are also few because of their significant incubation periods,

59 where melts can be held for significant times below their liquidi and not produce

60 recognizable crystals (Winkler 1947; Schairer and Bowen 1956; Fenn 1977; Lofgren

61 1974; Swanson 1977). The incubation period is the time it takes a system to re-establish

62 an equilibrium cluster-size distribution in response to a sudden change in temperature or

63 pressure (Turnbull 1948). During that adjustment period, the likelihood that a cluster of

64 critical size can be formed is extremely low. Incubation periods thus introduce large

65 uncertainties in determining the onset of nucleation (e.g., Swanson 1977; Fenn 1977).

66   One way of overcoming some of the experimental limitations is to deduce

67 crystallization rates from natural samples. Natural lavas, for example, can crystallize

68   over much longer periods of time than experimental samples. Crystal–size distributions

69   (CSD) of natural samples have thus been used to infer crystallization rates (e.g., Marsh

70   1988, 1998, 2007; Cashman and Marsh 1988; Higgins 1999; Morgan et al. 2007). A

71   CSD is described using a population density function $n = \frac{dN}{dL}$, where N is the cumulative

72   number of crystals per unit volume and L is the linear crystal size. The slope and

73   intercept on a plot of ln (n) versus L contains information on the average nucleation rate

74   and average growth rate (e.g., Cashman and Marsh 1988). Use of such methods,

75   however, provides only time-averaged crystallization rates, and requires that the

76   temperature–time interval of crystallization can be constrained independently.

77   In this study we use a different approach to derive nucleation rates for spherulites in

78   rhyolite lavas. Spherulites – radiating aggregates of crystals – were analyzed in three

79   dimensions using x-ray computed tomography, providing the full size of each spherulite

80   and their volumetric number density. To interpret the size distributions in terms of

81   nucleation kinetics, we derive the time frame for nucleation and the thermal conditions

82   for crystallization from modeling geochemical gradients around the spherulites (Gardner

83   et al. 2012; Befus et al. 2015). We target spherulites in Yellowstone rhyolite obsidian

84   lavas, because they are all dense aggregates of radiating sanidine and quartz (plus minor

85   amounts of Fe-Ti oxides) that grew in high-silica rhyolite melt under similar thermal

86   histories. Many variables that impact crystallization kinetics are thus similar between

87   samples.

88

89   **METHODS**

90   Six fist-sized samples were collected from three different lava flows (Pitchstone

91   Plateau, Summit Lake, and Solfatara Plateau) for this study (Fig. 1). One sample was

92   collected from near the mapped vent region of each flow (Y–22, Y–80, Y–200; Table 1),

93   while the other three come from either the flow front (Y–202 from Summit Lake and Y–

94   142 from Solfatara Plateau) or a significant distance away from vent (Y–193 from

95   Pitchstone Plateau). These lavas erupted between ~70 and 120 ka (Christiansen 2001;

96   Christiansen et al. 2007). A rectangular block ~3 cm per side was sawed from each

97   sample, and scanned at the University of Texas High-Resolution X-ray Computed

98   Tomography (HRXCT) facility. The data were acquired using a Zeiss (formally Xradia)

99   microXCT 400 operating at 60 kV and 8W with a 0.35 mm SiO_2 X-ray prefilter. All

100   scans were reconstructed as 16bit TIFF stacks with a resulting voxel (3D pixel) resolution

101   of 25.07 μm. Spherulites in the resulting gray scale images do not contrast greatly from

102   the surrounding matrix as a result of similar attenuation values, which made automated

103   segmentation and analysis not viable. Instead, each scan was imported into Avizo 8.0 for

104   manual segmentation, utilizing various software tools built into the program (Figure 2).

105   Each spherulite was visually identified and segmented into 3 orthogonal slices; more

106   slices were used for relatively large spherulites and those not roughly spherical to better

107   capture their actual shapes. The slices were used to measure the full 3D dimensions of

108   each spherulite. When spherulites were touching, segmentation was used to manually

109   separate them before analysis. Once segmented, each was saved individually and

110   imported into the Blob3D software (Ketcham 2005) for data extraction (Figure 2). Best–

111   fit ellipsoids were fitted to the previously segmented slices to measure the volume of each

112   spherulite. Uncertainty on volume measurements is controlled by the voxel size relative

113   to the spherulite diameter, but is thought to be on order of about 1% of the total volume

114   (Hanna et al., 2015). A total of 480–1190 spherulites were measured in each sample

115   (Table 1).   For convenience, we report the equivalent spherical diameter for each

116   spherulite calculated from its volume.

117   Thick sections were cut from each sample block and polished for geochemical

118   analysis. One to three spherulites were targeted in each sample, chosen to cover a broad

119   range of sizes. Each section was orientated so that the centers of the targeted spherulites

120   were exposed. This was achieved by first knowing where targeted spherulites were in the

121   blocks, based on the CT scans, and then slowly grinding the section until the size of the

122   targeted spherulites stopped increasing, indicating that the center had been reached. The

123   geochemical analyses, which were measured along traverses perpendicular to the edge of

124   the spherulites, were thus perpendicular to the full diameter of the spherulite. The widths

125   of individual crystals inside spherulites were measured using a petrographic microscope.

126   To augment our dataset an additional 54 analyses of spherulite-matrix glass pairs are

127   included from 14 other samples from Yellowstone lavas (Befus et al. 2015; Befus,

128   unpublished data). We followed the same analytical methods as reported in Gardner et al.

129   (2012) and Befus et al. (2015).   Briefly, trace–element concentrations were measured

130   using LA-ICP-MS at the University of Texas at Austin, using a New Wave Research UP

131   193-FX fast excimer (193 nm wavelength, 4-6 ns pulse width) laser system coupled to an

132   Agilent 7500ce ICP-MS. Reference standards and rhyolite sections were sampled as line

133   scans (5 μm s^{-1}), using a rectangular 5 x 50 μm slit aperture oriented with long-axis

134   normal to the scan direction, which was orientated normal to the local margin of the

135   spherulite and glass (Figure 1). The ICP-MS monitored masses ^{7}Li, ^{11}B, ^{23}Na, ^{25}Mg, ^{29}Si,

136   ^{39}K, ^{45}Sc, ^{55}Mn, ^{59}Co, ^{85}Rb, ^{88}Sr, ^{133}Cs, ^{137}Ba, and ^{208}Pb at a reading every 3.73 μm.

137   Time-resolved intensities were converted to concentration (ppm) equivalents using Iolite

138   software (Univ. Melbourne), with ^{29}Si as the internal standard, and a Si index value of

139   35.8 wt.%.   Based on recoveries among analytes we conservatively assign 5% as relative

140   uncertainties.

141

SPHERULITES AND THEIR ASSOCIATED GEOCHEMICAL

GRADIENTS IN YELLOWSTONE RHYOLITIC LAVAS

144   Spherulites in all samples consist of radiating masses of intergrown sanidine and

145   quartz crystals, with minor amounts of Fe-Ti oxides and glass (Fig. 1).   In most cases,

146   sanidine and quartz crystals are elongated roughly perpendicular to the outer margin of

147   the spherulite (Fig. 3).   In the cores of the largest spherulites individual crystals are 29±5

148   μm wide.   Near the rims of those same spherulites, however, individual crystals are only

149   8±2 μm wide. In the smallest spherulites, crystals are smaller, 10±3 μm and 7±1 μm in

150   spherulite cores and rims, respectively.   Note that crystals throughout small spherulites

151   are similar in size to those near the rims of large spherulites (Fig. 3).

152   The largest spherulites measured have volumes that range from 17.6 to 459.9 mm^3,

153   depending on the sample (Table 1).   The smallest spherulites measured have volumes

154   ranging from 0.0057 to 0.013 mm^3.   There are smaller spherulites in all samples, but

155   these were smaller than analytical resolution.   We note that their numbers are few

156   compared to the measured population of spherulites, as shown by the size distributions

157   (Figure 4).   Overall, the equivalent spherical diameter of spherulites ranges from ~220 to

158   ~9580 μm. The median volume is ~0.191 to ~0.996 mm^3, or ~715 to ~1240 μm in

159   diameter.

160   Spherulite size distributions are mainly unimodal, with the most common spherulites

161   in all samples being ~660–1020 μm in diameter (Figure 4). These make up ~50–60% of

162   the populations in the Pitchstone Plateau and Solfatara Plateau samples and ~35–40% of

163   the Summit Lake samples. All populations are positively skewed, with relatively large

164   spherulites making up different proportions of the populations in different samples. For

165   example, spherulites larger than 880 μm make up 24–29% of the populations in the

166   Summit Lake samples, but only 2–17% in the others. In general, Summit Lake samples

167   contain larger spherulites, and in fact one sample (Y202) has a secondary mode in size at

168   ~1500 μm. Despite such differences, number densities of spherulites from all three flows

169   overlap, and range from ~74 to ~314 cm^{-3} (Table 1).

170   A total of 63 spherulite–matrix glass pairs were analyzed, and all show similar

171   geochemical patterns (Figure 5). Concentrations of Li are uniformly low within

172   spherulites (7±4 ppm), and uniformly high in the surrounding glass (58±5 ppm). The

173   change is sharp, occurring over a distance of <10 μm, and coincides with the margin of

174   the spherulite. Concentrations of Rb are also relatively low inside spherulites (113±33

175   ppm), and larger spherulites typically have slightly less Rb in them than smaller ones.

176   Far away from spherulites the glasses in all samples have uniformly high Rb contents of

177   225±22 ppm (Figure 5). Unlike Li, Rb contents vary in the matrix, with the maximum

178   concentration occurring at the contact with the spherulite and decreases over a distance of

179   ~190–390 μm to the far–field value (Figure 5). Both the enrichment of Rb at the margin

180   and the distance over which elevated concentrations are found in the glass correlate with

181   the size of the spherulite. Measured concentrations of Rb for all spherulite – matrix pairs

182   are listed in the Supplemental Data Table. It is thought that Rb inside the spherulites is

183   contained in the feldspars and/or any remaining glass. All other elements have variable

184   but similar abundances inside and outside of the spherulites (Figure 5). There are spikes

185   in concentrations found at the outer edges of some spherulites, most commonly in Mg,

186   Cs, Ba, Sr, and Pb.

187

188   **DISCUSSION**

189   The fact that spherulites of all sizes are approximately spherical indicates that they

190   grew after lava has been emplaced and ceased to deform. Because all spherulites in a

191   given sample experience the same thermal history, it is reasonable to assume that (i) all

192   spherulites in a given sample stopped growing at the same time/temperature, and (ii)

193   larger spherulites are larger because they nucleated earlier, and thus at higher

194   temperature, and were growing for longer periods of time than smaller spherulites. Thus,

195   with knowledge of spherulite growth rates and thermal histories, one can use spherulite

196   size distributions to reconstruct nucleation rate versus temperature curves.

197   Recent studies have shown that compositional gradients associated with spherulites in

198   rhyolitic lavas formed during their growth while the lava cooled (Castro et al., 2009;

199   Watkins et al., 2009; Gardner et al., 2012; Befus et al., 2013; Befus, 2016). The style of

200   gradient for a given element can be understood in terms of its relative compatibility and

201   diffusivity, growth kinetics of the spherulite, and the thermal conditions of the lava

202   (Smith and Tiller 1955; Albarende 1972; Skora 2006; Watson and Muller 2009; Gardner

203   et al. 2012; Befus et al., 2015). Briefly, while lava cools elements that diffuse fast

204   relative to the growth rate of the spherulite are expected to have different abundances

205   inside and outside of the spherulite, based on their compatibility with the crystals forming

206   the spherulite, but there will be no gradients in concentration in either; for convenience,

207   we refer to these as Type 1 gradients.   On the other hand, elements that diffuse

208   significantly slower than the spherulite grows are expected to have constant abundances

209   across the spherulite and matrix, which we refer to as Type 3 gradients. In between, there

210   are some incompatible elements that can diffuse slightly faster than the spherulite can

211   grow, and hence they become concentrated at the migrating spherulite–matrix boundary.

212   The elevated concentrations lead to diffusion away from the boundary, resulting in

213   decreasing concentrations out into the glass until the far-field concentration is reached;

214   we refer to these gradients as Type 2. Studies of spherulites in rhyolite lavas indicate that

215   concentrations of Rb and H_2O commonly occur in Type 2 gradients (Castro et al. 2008;

216   Watkins et al. 2009; Gardner et al. 2012; Befus et al. 2015).

217   Compositional gradients can be modeled using a moving boundary diffusion model

218   that incorporates the growth rate of the spherulite, thermal conditions during its growth,

219   and the diffusion rate of the element (Gardner et al., 2012). Here, we use a model in

220   which radial spherical growth decreases as a function of temperature, following

221

222         $$\left(\frac{dR}{dt}\right) = \left(\frac{dR}{dt}\right)_O *exp\,[-a*(T - T_O)]$$ (1)

223

224   where $\left(\frac{dR}{dt}\right)$ is the radial growth rate at a specific timestep, $\left(\frac{dR}{dt}\right)_O$ is the initial radial

225   growth rate, T is temperature at time t, and T_O is initial temperature. The parameter a is

226   set to 0.025 to generate an exponential decay in growth rate (Befus et al., 2015). This

227   growth model was shown to best fit the overall differences in elemental enrichment at

228   spherulite–matrix boundaries of spherulites in rhyolite lava (Gardner et al., 2012; Befus

229   et al., 2015). As a point of reference, we report growth rate $\left(\frac{dR}{dt}\right)$ at 600 °C, but

230   emphasize that growth rate is not constant in the model, but instead slows as lava cools.

231   Temperature of the cooling lava is modeled as a function of time (t) as it changes

232   from T_O to the temperature at which spherulites cease growing (T_F), following

233

234        $$T = T_O \exp[-(bt)^{1.5}]$$ (2)

235

236   where b is a fit parameter. This functional form reproduces the shape of the temperature-

237   time path of numerical conductive cooling models of lava (Manley, 1992; Gardner et al.,

238   2012). All magmas of interest were stored at 750±25 °C (Befus and Gardner, 2016), and

239   so we set $T_O = 750$°C.

240   In all calculations the diffusivity (D) for each element varies as a function of

241   temperature, following the model equations proposed by Zhang et al. (2010) for rhyolitic

242   melts. In most cases, the equation for D takes the form

243

244        $$D = \exp\left[c - \frac{d}{T}\right]$$ (3)

245

246   where c and d are fit parameters based on experimental data.

247   Gardner et al. (2012) showed that, for a given growth rate, gradients in the

248   concentrations of incompatible elements are expected to evolve from Type 3 to Type 2 to

249   Type 1 as either cooling rate slows or T_O increases. A similar evolution is expected as

250   growth rate increases under a given thermal regime. Of the elements analyzed, Li is the

251   only one that occurs in Type 1 profiles (Figure 5). Using the diffusivity model for Li in

252   Zhang et al. (2010), and assuming reasonable estimates for cooling and growth rates

253   (Befus et al., 2015), the occurrence of Li in Type 1 profiles suggests that all spherulites

254   grew when $T > 350$ °C. If they had continued to grow at much colder temperatures, Li

255   diffusion would become slow enough relative to spherulite growth that it would form

256   Type 2 gradients. Most other elements of interest form Type 3 gradients, with equal

257   concentrations inside and outside of the spherulite. Of those that form Type 3, Sr is

258   expected to diffuse the fastest at relevant conditions, based on the models of Zhang et al.

259   (2010). If $T > 700$ °C, however, Sr diffusion would become fast enough that it would be

260   expected to form Type 2 gradients. The absence of such gradients for Sr concentrations

261   thus argue that spherulites grew at temperatures of 700 °C or colder. We thus assume

262   that most spherulites grew while temperature was between ~350 °C and ~700 °C.

263   Support for those relatively cold temperatures for growth of Yellowstone spherulites

264   comes from the observation that they all crosscut flow banding in the samples, instead of

265   deflecting or distorting it. The lack of deflection argues that the Yellowstone spherulites

266   grew while the lava was instead glassy, and hence when temperature was below the glass

267   transition (T_g). If spherulites grew while the lava was still molten, then their growth

268   tends to deflect flow banding (Castro et al. 2008; Watkins et al. 2009; van Aulock et al.

269   2013). For Yellowstone rhyolite, T_g is estimated at 610–700°C, using the viscosity model

270   of Giordano et al. (2008) and assuming that $T_g \sim T$ at which viscosity $= 10^{12}$ Pa s. That

271   suggests that most spherulites nucleated and grew at temperatures below ~600 °C.

272   Both the growth history of a spherulite and the thermal conditions during its growth

273   are recorded in the relative enrichment of Type 2 elements, and how far those elements

274   diffuse away from the margin (Watson and Müller, 2009; Gardner et al. 2012; Befus et al.

275   2015). Here, we define Rb enrichment (ε) as the ratio of its maximum concentration at

276   the margin to its far-field concentration in the matrix, and then convert it to a percentage.

277   The distance away from the spherulite margin that Rb is enriched above the far-field

278   concentration is defined as its propagation distance (P_Δ). We calculate P_Δ as the distance

279   from the margin that the Rb concentration is greater than two standard deviations above

280   that measured in the far-field matrix (Befus et al. 2015). Befus et al. demonstrated that

281   the ratio $\left(\frac{\varepsilon}{P_\Delta}\right)$ is greater for spherulites that grow faster, at a given cooling rate (Figure

282   6a). Conversely, $\frac{\varepsilon}{P_\Delta}$ decreases for slower cooling rate, for a given growth rate.

283   The ratio $\frac{\varepsilon}{P_\Delta}$ has been calculated for every spherulite-glass pair and is plotted versus

284   the size of the spherulite in Figure 6. Also shown are $\frac{\varepsilon}{P_\Delta}$ versus radius for model

285   spherulites, with each curve representing iterative solutions to the numerical moving

286   boundary diffusion modeling using Equations 1-3. Curves in Figure 6 labeled with

287   growth rates were constructed by specifying a growth rate, and solving the equations for

288   a range of possible cooling rates. Curves labeled with cooling rates were each calculated

289   by fixing cooling rate and systematically changing growth rate. The cloud of data

290   formed by the samples covers permissible ranges for parameters in equations (1) and (2).

291   For temperature, the "permissible" range for $b = 3.3$ to 32.7, corresponding to cooling

292   rates of 0.0063 to 0.063 °C hr^{-1}. Regression of the entire set gives a best fit for $b =$

293    $9.5^{+14.5}_{-3.0}$, which equals a cooling rate solution of $0.60^{+0.6}_{-0.3}$ °C day^{-1}. When b is set to 9.5

294   and $\left(\frac{dR}{dt}\right)_O$ is modified in the growth law equation, the full range of data can be explained

295   by $\left(\frac{dR}{dt}\right)$ between 0.2 to 2.0 μm hr^{-1}, with the entire set best fit by a growth rate of 1.0±0.5

296   μm hr^{-1}, again defined as the value at 600 °C, recognizing that the rate decreases

297   exponentially with decreasing T.

298

299   **Nucleation Temperatures of Spherulites**

300   We can determine the temperature at which each spherulite nucleated by assuming a

301   given cooling rate and specifying a growth rate. Our modeling of compositional

302   gradients surrounding spherulites indicates that all spherulites grew on average at 1 μm

303   hr^{-1} (when T = 600 °C), while the lavas cooled at a rate of ~0.6 °C day^{-1}. Cooling

304   temperatures and slowing growth with time is supported by the observation that crystal

305   sizes in large spherulites decrease from their interiors to their rims (Fig. 3). In addition,

306   small spherulites, thought to nucleate at colder temperatures than large ones, are fine

307   grained like those in the outer parts of the large spherulites.

308   Based on the average rates of growth and cooling, the sizes of spherulites in each

309   sample suggest that nucleation temperature ranges between 480 and 600°C (Figs. 7, 8).

310   Those temperatures vary, however, if the rates of cooling and growth differ. Spherulites

311   would need to nucleate at hotter temperatures if they grew more slowly under faster

312   cooling. Indeed, given the spread in rates inferred from the compositional gradients

313   (Figures 6a,b), spherulites would have nucleated at 590–710°C under the fastest cooling

314   and slowest growth permissible. Conversely, spherulites would nucleate at colder

315   temperatures if they grew faster under slower cooling, and in fact under the slowest

316   permissible cooling and fastest growth, they would have nucleated at 430–500°C.

317

Nucleation Rates of Spherulites

319   Our modeling suggests that spherulites of similar size nucleate at about the same

320   temperature (Figure 7a). We thus arbitrarily group spherulites together that nucleated

321   within a temperature window of 10 °C, which defines the number of spherulites

322   nucleated per 10° C (Figure 7b). The cooling rate of the sample defines the amount of

323   time that lapsed between each 10 °C interval. As for the volume in which spherulites can

324   nucleate, it shrinks over time as previously nucleated spherulites continue to grow.

325   Because no spherulites were seen to have grown inside other ones, we can assume that

326   the final volume of each spherulite after it stops growing equals the volume in which no

327   later spherulite could have nucleated. This is the same as saying that there is a halo of

328   matrix around a growing spherulite in which no other spherulite can nucleate. The

329   "effective" volume available for nucleation at any given time (temperature) thus equals

330   the total sample volume minus the sum of the final volumes of all spherulites that had

331   nucleated previously (at higher temperature). The reported nucleation rate for each

332   sample is the number of spherulites nucleated in 10 °C intervals per effective unit volume

333   per unit time (Figure 7c).

334   We calculate nucleation rates for the six samples separately to establish the range in

335   rates (Figure 9). Assuming best–fit rates for growth and cooling (Figure 6), nucleation,

336   on average, begins at 592±8°C, and the rate of nucleation accelerates greatly to a peak of

337   0.072 ± 0.049 cm^{-3} hr^{-1} at 533±14°C. Upon further cooling, nucleation slows until it

338   ceases at 485±6°C. More generally, nucleation rate depends on assumed rates of cooling

339   and growth. Under the fastest permissible cooling, peak nucleation rates increase to

340   0.232($\pm$0.163) to 0.245($\pm$0.180) cm^{-3} hr^{-1}, depending on growth rate. Under conditions of

341   extremely slow cooling, nucleation rate slows to 0.025($\pm$0.018)–0.028($\pm$0021) cm^{-3} hr^{-1}.

342   The distribution of nucleation rates for most samples is unimodal, and only slightly

343   skewed toward higher temperature. In one case (Y202), however, there is a bimodal

344   distribution of nucleation rates spread out over a wider range of temperatures.   The

345   secondary peak at higher temperature is the reflection of a greater number of large

346   spherulites in that sample.

347   Crystals nucleate in melt/glass at temperatures below the liquidus temperature (T_L),

348   which is defined as the degree of undercooling, ΔT ($= T_L - T$) (e.g., Lofgren, 1971). For

349   the sanidine+quartz spherulites in Yellowstone lavas we assume that T_L equals the

350   highest temperature at which both sanidine and quartz crystallize together. Quartz joins

351   sanidine as a crystallizing phase at ~800°C at 25 MPa in hydrous Yellowstone rhyolite

352   (Befus and Gardner, 2016). Extrapolating to 0.1 MPa places the upper limit of their co-

353   precipitation at slightly above 800°C, because the stability curve for quartz is nearly

354   vertical in pressure-temperature space.   We thus assume that T_L for Yellowstone

355   spherulites is 800°C.   Given that assumption, spherulites nucleated under best–fit

356   conditions at $\Delta T \approx 208(\pm 6)$–315($\pm 8$)°C (Figure 9). More generally, $\Delta T \approx 100$–203°C to

357   277–365°C, given the permissible ranges in the rates of growth and cooling rate.

358   Regardless of absolute values of ΔT, however, the nucleation interval spans a temperature

359   range of roughly ~88–113°C.

360   The peak in spherulite nucleation is inferred by this study to have occurred at $\Delta T =$

361   155(± 14)–331(± 16)°C for the ranges in rates of growth and cooling.   Under best–fit

362   conditions, $\Delta T = 267(\pm 14)$°C. Overall, therefore, nucleation begins when $\Delta T \approx 0.65$–0.88

363    $\times T_L$, and peaks when $\Delta T \approx 0.59\text{--}0.80 \times T_L$. The peak rate thus occurs at $\Delta T \approx \frac{2}{3} T_L$,

364   which is expected from classical nucleation theory (Lasaga 1998). We note that almost

365   all relatively large spherulites have some phenocryst in their cores, and thus seem to have

366   nucleated heterogeneously.

367

368   **COMPARISON TO PREVIOUS STUDIES**

369   Recently, Befus (2016) measured oxygen isotopic fractionation between quartz and

370   alkali feldspar ($\Delta^{18}O_{Qtz\text{-}Kfs}$) in Pitchstone Plateau spherulites and found that $\Delta^{18}O_{Qtz\text{-}Kfs}$ is

371   1.3±0.7‰ in their cores. Such fractionation implies the spherulites nucleated at 578±160

372   °C. It was also found that $\Delta^{18}O_{Qtz\text{-}Kfs}$ increases to 2.9±1.1‰ near spherulite rims, which

373   implies that spherulites continued to grow until 301±88 °C, well below T_g. The

374   agreement in nucleation temperatures and the thermal regime for growth between the

375   studies (Figure 8), which used independent methods, lends strong support to the

376   nucleation rates derived in this study.

377   In an experimental decompression study of the crystallization of Yellowstone

378   rhyolite, Befus et al. (2015) found that alkali feldspar microlites nucleated at $\Delta T \geq 60°C$,

379   but only after 24–120 hours at low pressure. Clinopyroxene nucleated under similar

380   conditions as alkali feldspar. In this case, crystallization was driven by loss of dissolved

381   H_2O from the melt, and thus ΔT equates to how much the mineral liquidus temperature is

382   raised above the experimental temperature (Hammer and Rutherford, 2002; Befus et al.,

383   2015). Quartz joined alkali feldspar only when ΔT reached $\geq 120°C$, and they co–

384   precipitated in coarse crystal aggregates that appear granophyric in texture. They did not

385   form spherical aggregates of closely packed crystals. Our results are consistent with

386   these experimental results, in that dense spherulites appear to require significantly higher

387   ΔT to nucleate and grow. Indeed, Befus et al. (2015) demonstrated that most microlites

388   in the matrix of Yellowstone lavas grew before lava emplacement, and hence prior to the

389   development of spherulites.

390   Experimental studies of igneous textures, especially in rhyolitic melts, often only

391   report nucleation densities, because of the uncertainties in conditions for nucleation.

392   Swanson (1977) reported number densities of feldspars and quartz nuclei in hydrous

393   silicic melts, and found that they increased dramatically as ΔT increased, from <10 cm^{-3}

394   at $\Delta T < 100°C$ to $>10^{7-8}$ cm^{-3} at $\Delta T > 200°C$. Fenn (1977) reported nucleating $10^3–10^{3.8}$

395   feldspar spherulites per cm^{-3} in hydrous feldspathic melt at $\Delta T \geq 110°C$. In comparison,

396   spherulites in Yellowstone lavas occur in number densities of 74 to 314 cm^{-3}, and

397   nucleated at $\Delta T = 100–365°C$. The significantly lower nucleation density at greater ΔT

398   for natural rhyolite can most likely be attributed to the impact of dissolved H_2O on

399   nucleation rate. Both Fenn (1977) and Swanson (1977) used melts with ~2–12 wt.%

400   H_2O, which is significantly more than that in matrix glasses of Yellowstone lavas (~0.1–

401   0.2 wt.%). Greater H_2O contents are known to significantly accelerate diffusion (Zhang

402   et al. 2007) and lower viscosity (Giordano et al., 2008), both of which enhance nucleation

403   (e.g., Swanson and Fenn 1986). Greater H_2O contents also lowers T_g (Deubener et al.,

404   2003), which would allow spherulites to nucleate while rhyolite is still molten, also

405   enhancing nucleation.

406   Spherulites grown experimentally generally change in texture from coarse and open

407   at low ΔT, to "bow tie" shaped at moderate ΔT, to round and dense with small crystals at

408   high ΔT (Lofgren 1971; Swanson 1977; Swanson et al. 1989). The latter type tend to

409   grow at ΔT > 250–300°C (Lofgren 1971; Swanson 1977). Yellowstone spherulites are

410   generally spherical and closely packed with small crystals (relative to the size of the

411   spherulite) and lack obvious bow-tie structures (Figure 1). It is noteworthy that dense,

412   fine-grained Yellowstone spherulites are inferred to have grown at ΔT of ~250°C, similar

413   to experiments, despite differences between experimental and natural samples.

414

CONCLUSIONS

416   Spherulites measured in Yellowstone obsidian lavas range in size from 0.006 to 460

417   mm^3, with median volumes of 0.19–0.99 mm^3. Geochemical gradients preserved around

418   spherulites indicate that most grew while the lavas cooled at 0.30 to 1.20 °C day^{-1}, at

419   rates that decreased exponentially with temperature and time, but were 0.2 to 2.0 $\mu m\ hr^{-1}$

420   at 600°C. Between 74 and 314 cm^{-3} spherulites nucleated during cooling, and mostly

421   formed unimodal, symmetrical distribution of sizes. Growth occurred over a range of

422   temperatures, consistent with the variations in crystal sizes, and mostly at or below the

423   glass transition temperature of the matrix, consistent with the lack of deformation of the

424   matrix by the spherulites.   Depending on rates of cooling and growth, nucleation

425   temperatures fall between ~430 to ~710°C, but the actual range in temperature is much

426   narrower for a specific set of conditions. Peak nucleation rates of 0.072±0.049 $cm^{-3}\ hr^{-1}$

427   are found at ΔT = 267(±14)°C, using best-fit approximations for the rates of cooling and

428   growth. The nucleation rates derived in this study provide estimates that are appropriate

429   for nearly anhydrous rhyolite, which have not been measured experimentally.

430

441
442 **REFERENCES CITED**

443 Befus, K.S. (2016) Crystallization kinetics of rhyolitic melts using oxygen isotope ratios,
444   Geophysical Research Letters, 43, doi:10.1002/2015GL067288.
445 Befus, K.S., and Gardner, J.E. (2016) Magma storage and evolution of the most recent
446   effusive and explosive eruptions from Yellowstone caldera. Contributions to
447   Mineralogy and Petrology, doi: 10.1007/s0041-016-1244-x.
448 Befus, K.S., Manga, M., Gardner, J.E., and Williams, M. (2015) Ascent and
449   emplacement dynamics of obsidian lavas inferred form microlite textures. Bulletin of
450   Volcanology, 77, doi:10.1007/s00445–015–0971–6.
451 Befus, K.S., Watkins, J., Gardner. J.E., Richard, D., Befus, K.M., Miller, N.R., and
452   Dingwell, D.B. (2015) Spherulites as in-situ recorders of thermal history in lava
453   flows. Geology, 43, 647–650.
454 Bowen, N.L. (1919) Crystallization differentiation in igneous magmas. Journal of
455   Geology, 27, 393–430.
456 Bowen, N.L. (1947) Magmas. Bulletin of the Geological Society of America, 58, 263-
457   280.
458 Cashman, K.V., and Marsh, B.D. (1988) Crystal size distribution (CSD) in rocks and the
459   kinetics and dynamics of crystallization; 2, Makaopulu lava lake. Contributions to
460   Mineralogy and Petrology, 99, 292–305.
461 Castro, J.M., Beck, P., and Tuffen, H. (2008) Timescales of spherulite crystallization in
462   obsidian inferred from water concentration profiles. American Mineralogist, 93,
463   1816–1822.
464 Christiansen, R.L. (2001) The Quaternary and Pliocene Yellowstone Plateau Volcanic
465   Field of Wyoming, Idaho, and Montana. United States Geological Survey
466   Professional Paper 729–G, 145 p.
467 Christiansen, R.L., Lowenstern, J.B., Smith, R.B., Heasler, H., Morgan, L.A., Nathenson,
468   M., Mastin, L.G., Muffler, L.J.P., and Robinson, J.E. (2007) Preliminary assessment
469   of volcanic and hydrothermal hazards in Yellowstone National Park and vicinity.
470   United States Geological Survey Open-file Report 2007-1071, 94 p.
471 Deubener, J., Müller, R., Behrens, H., and Heide, G. (2003) Water and the glass
472   transition temperature of silicate melts. Journal of Non–Crystalline Solids, 330, 268–
473   273.
474 Fenn, P.M. (1977) The nucleation and growth of alkali feldspars from hydrous melts.
475   Canadian Mineralogist, 15, 135-161.
476 Gardner, J.E., Befus, K.S., Watkins, J., Hesse, M., and Miller, N. (2012) Compositional
477   gradients surrounding spherulites in obsidian and their relationship to spherulite
478   growth and lava cooling. Bulletin of Volcanology, 74, 1865–1879.
479 Giordano, D., Russell, J.K., and Dingwell, D.B. (2008) Viscosity of magmatic liquids: A
480   model. Earth and Planetary Science Letters, 271, 123-134.
481 Hammer, J.E., and Rutherford, M.J. (2002) An experimental study of the kinetics of
482   decompression–induced crystallization in silicic melt. Journal of Geophysical
483   Research, 107, doi:10.1029/2001JB000281.

484   Hanna, R.D., Ketcham, R.A., Zolensky, M., and Behr, W.M. (2015) Impact–induced
485   brittle deformation, porosity loss, and aqueous alteration in the Mutchison CM
486   chondrite. Geochimica Cosmochimica Acta, 171, 256–282.
487   Higgins, M.D. (1999) Origin of megacrysts in granitoids by textural coarsening: A crystal
488   size distribution (CSD) study of microcline in the Cathedral Peak granodiorite, Sierra
489   Nevada, California. Geological Society of London Special Publications, 168, 207–
490   219.
491   Johannes, W. (1979) Ternary feldspars: Kinetics and possible equilibria at 800°C.
492   Contributions to Mineralogy and Petrology, 68, 221–230.
493   Ketcham, R.A. (2005) Computational methods for quantitative analysis of three-
494   dimensional features in geological specimens. Geosphere, 1, 32-41.
495   Lasaga, A.C. (1998) Kinetic theory in the earth sciences. Princeton University Press,
496   Princeton, N.J., 811 p.
497   Lofgren, G. (1971) Experimentally produced devitrification textures in natural rhyolitic
498   glass. Bulletin of the Geological Society of America, 82, 111-124.
499   Lofgren, G.E. (1974) An experimental study of plagioclase crystal morphology:
500   isothermal crystallization. American Journal of Science, 274, 1974.
501   Manley, C.R. (1992) Extended cooling and viscous flow of large, hot rhyolite lavas:
502   Implications of numerical modeling results. Journal of Volcanology and Geothermal
503   Research, 53, 27–46.
504   Marsh, B. (1988) Crystal size distribution (CSD) in rocks and the kinetics and dynamics
505   of crystallization. Contributions to Mineralogy and Petrology, 99, 277–291.
506   Marsh, B. (1998) On the interpretation of crystal size distributions in magmatic systems.
507   Journal of Petrology, 39, 553–599.
508   Marsh, B.D., Crystallization of silicate magmas deciphered using crystal size
509   distributions. Journal of the American Ceramics Society, 90, 746–757, 2007.
510   McKenzie, D. (1984) The generation and compaction of molten rock. Journal of
511   Petrology, 25, 713–765.
512   Morgan, D.J., Jerram, D.A., Chertkoff, D.G., Davidson J.P., Pearson, D.G., Kronz, A.,
513   and Nowell, G.M. (2007) Combining CSD and isotopic microanalysis: magma supply
514   and mixing processes at Stromboli Volcano, Aeolian Islands, Italy. Earth and
515   Planetary Science Letters, 260, 419–431.
516   Schairer, J.F., and Bowen, N.L. (1956) The system $Na_2O–Al_2O_3–SiO_2$. American
517   Journal of Science, 254, 129–195.
518   Swanson, S.E. (1977) Relation of nucleation and crystal-growth rate to the development
519   of granitic textures. American Mineralogist, 62, 966-978.
520   Swanson, S.E., and Fenn, P.M. (1986) Quartz crystallization in igneous rocks. American
521   Mineralogist, 71, 331-342.
522   Swanson, S.E., Naney, M.T., Westrich, H.R., and Eichelberger, J.C. (1989)
523   Crystallization history of Obsidian Dome, Inyo Domes, California. Bulletin of
524   Volcanology, 51, 161–176.
525   Turnbull, D. (1948) Transient nucleation. Transactions of the American Institute of
526   Mineral Engineering, 175, 174-783.
527   von Aulock, F.W., Nichols, A.R.L., Kennedy, B.M., and Oze, C. (2013) Timescales of
528   texture development in a cooling lava dome. Geochimica et Cosmochimica Acta, 114,
529   72–80.

530   Watkins, J., Manga, M., Huber, C., and Martin, M. (2009) Diffusion-controlled spherulite
531   growth in obsidian inferred from H2O concentration profiles. Contributions to
532   Mineralogy and Petrology, 157, 163–172.
533   Winkler, H.G.F. (1947) Kristallogrosse und Abkuhlung. Heidelberger Beitr. Mineralogie
534   und Petrology, 1, 86-104.
535   Zhang, Y., Ni, H., and Chen, Y. (2010) Diffusion data in silicate melts. Reviews in
536   Mineralogy and Geochemistry, 72, 311-408.
537

538
539   **FIGURE CAPTIONS**

540

541   **FIGURE 1. a)** Simplified geologic map of Central Plateau Member rhyolites in the

542   Yellowstone caldera, WY, modified after Christiansen (2001). Lava flows are shown in

543   pink, with sampled lavas labeled, and positions where samples were collected (black

544   squares for samples scanned by HRXCT; gray circles are additional samples for

545   geochemical data; white circle is Y24 from Befus et al. (2015), also included in this

546   study. **b)** Representative photograph of Yellowstone spherulites from Solfatara Plateau

547   lava, photographed near Y142 in **a)**. Field of view is approximately 10 cm across. **c)**

548   Photomicrograph of a representative spherulite (in sample Y202) analyzed for

549   geochemical gradients. For scale, the laser track highlighted is 100 μm wide. The

550   gradation in color in the spherulite probably results from oxidation.

551

552   **FIGURE 2.** Image illustrating steps used to measure spherulite volumes. **a)** and **b)**

553   crystals in the core and rim, respectively, of spherulite Y80 T1, which is 2950 μm in

554   diameter. Scale bar is 200 μm long. **c)** crystals in spherulite Y80 T2, which is 300 μm in

555   diameter. Scale bar is 100 μm long.

556

557   **FIGURE 3.** Photomicrographs of crystals in Yellowstone spherulites. **a)** spherulites

558   manually segmented in Aviso using three orthogonal planes to represent their volumes,

559   shown in relationship to a tomography slice. **b)** segmented planes were transported into

560   Blob3D to verify that all spherulites were separated. **c)** best-fit ellipsoids for each

561   spherulite were generated using Blob3D

562

563   **FIGURE 4.** Spherulite size distributions. **a)** Y22; **b)** Y80; **c)** Y142; **d)** Y193; **e)**

564   Y200; and **f)** Y202.

565

566   **FIGURE 5.** Example concentrations of Li, Rb, and Sc in spherulite and matrix glass

567   as a function of distance. The boundary between spherulite and matrix is marked with

568   the dotted lines. The left-hand column shows elemental concentrations associated with

569   Y193 T1 (585 μm diameter); the right-hand column is Y142 T1 (2030 μm diameter).

570   The enrichment (ε) of Rb at the margins and the propagation distance (P_Δ in μm) are

571   listed for each. Predicted variations in Rb concentration from the moving boundary

572   diffusion model are shown as gray curves, calculated using best-fit rates for growth

573   (1.0 ± 0.5 μm hr^{-1}) and cooling ($10^{-1.6\pm0.3}$ °C hr^{-1}).

574

575   **FIGURE 6.** The ratio of Rb enrichment (ε) to propagation distance (P_Δ) for 63

576   spherulite − matrix glass pairs as a function of the diameter of the spherulite measured in

577   20 samples from the three targeted lava flows (see Figure 1). Black squares are data from

578   the samples scanned by HRXCT, gray circles are data from other spherulites (Befus,

579   unpublished data) and white circles are data from Befus et al. (2015). Red square is

580   spherulite Y142 T1 and green square is Y193 T1 (Fig. 4). **a)** Variations in the ratio

581   expected as a function of cooling rate and growth rate are shown as curves. The best-fit

582   rates for the entire dataset are solid curves, whereas dashed curves show the range of

583   permissible rates. **b)** Variations in the ratio expected given the best-fit cooling rate, for

584   different growth rates (solid curves) and nucleation temperatures (dashed curves).

585

586   **FIGURE 7.** Example output for sample Y142, using the best-fit growth rate and

587   cooling rate. **a)** Nucleation temperature calculated for each spherulite in the sample, once

588   growth rate and cooling rate are specified. **b)** histogram of numbers of spherulites

589   nucleated in intervals of 10 °C. **c)** Volumetric nucleation rate for each bin in (b)

590   calculated with knowledge of the sample size (spherulites + glass) and the amount of time

591   lapsed between each 10 ºC interval of cooling.

592

593   **FIGURE 8.** Frequency of nucleation temperatures (°C) for spherulites. **a)** Y22; **b)**

594   Y80; **c)** Y142; **d)** Y193; **e)** Y200; and **f)** Y202.

595

596   **FIGURE 9.** Nucleation Rates of spherulites for the six Yellowstone rhyolite samples

597   as functions of undercooling ΔT [= $T_{liquidus} - T_{nucleation}$, with $T_{liquidus}$ assumed to be 800°C].

598

599

600

601

TABLE 1: SPHERULITE SIZES AND AMOUNTS

Sample	Average[a] (mm^3)	Median[a] (mm^3)	Largest[a] (mm^3)	Smallest[a] (mm^3)	N_S[b] (cm^{-3})	n[c]	ϕ[d] (vol.%)
Y22	0.9726	0.3551	28.74	0.0074	256.2	652	13.70
Y80	0.4624	0.1910	17.59	0.0057	314.4	1190	14.53
Y142	0.9757	0.3073	49.60	0.0120	125.5	809	12.24
Y193	2.1535	0.4371	58.37	0.0140	74.4	480	16.02
Y200	3.3506	0.6644	120.4	0.0100	88.0	489	29.47
Y202	3.2969	0.9961	459.9	0.0130	110.1	525	36.28

[a]Average, Median, largest, smallest volumes of spherulites, in cubic millimeters.

[b]N_S = number density of spherulites, in number per cubic centimeters.

[c]n = number of spherulites measured.

[d]ϕ = volume percent of spherulites in the sample.
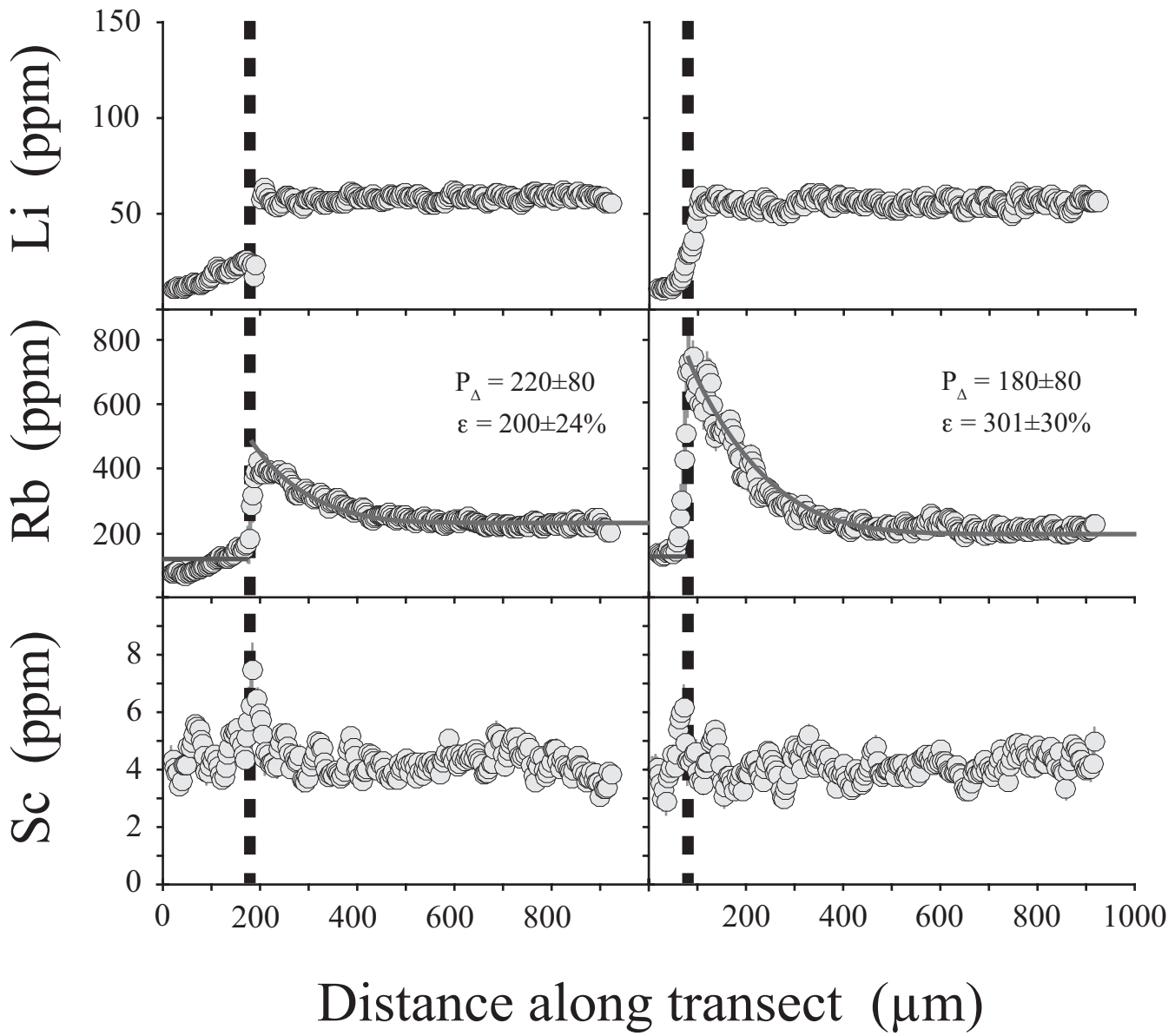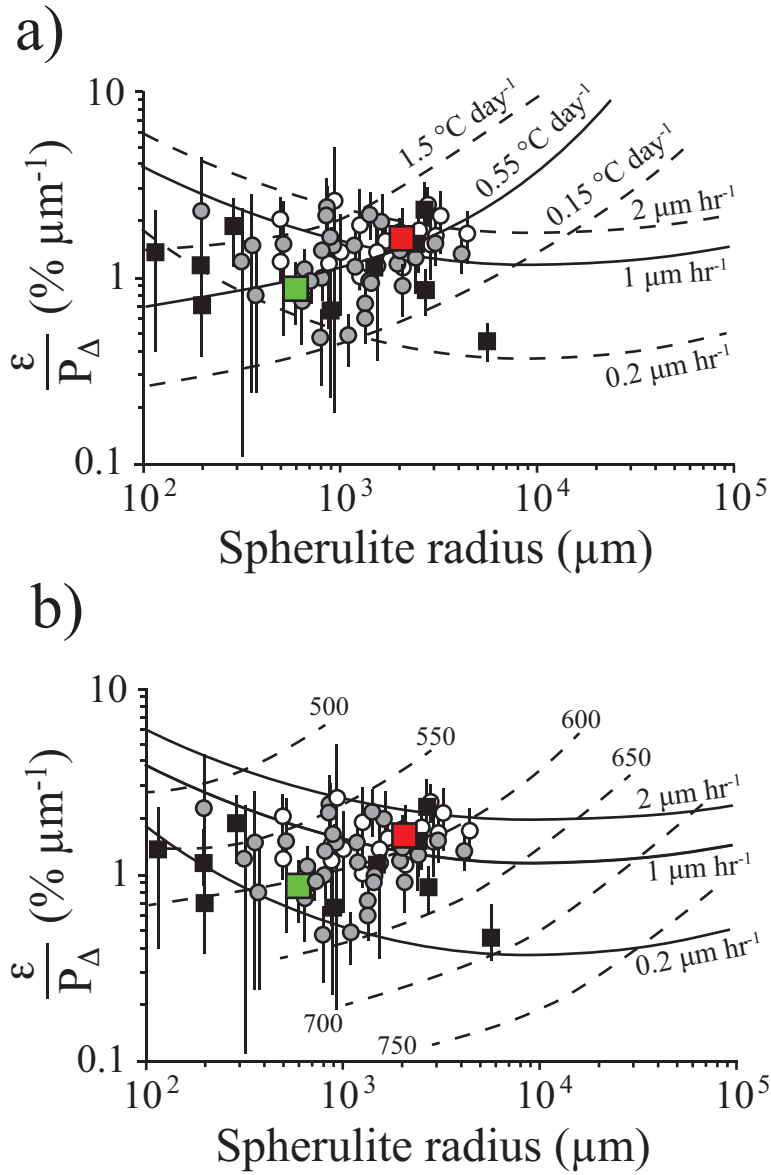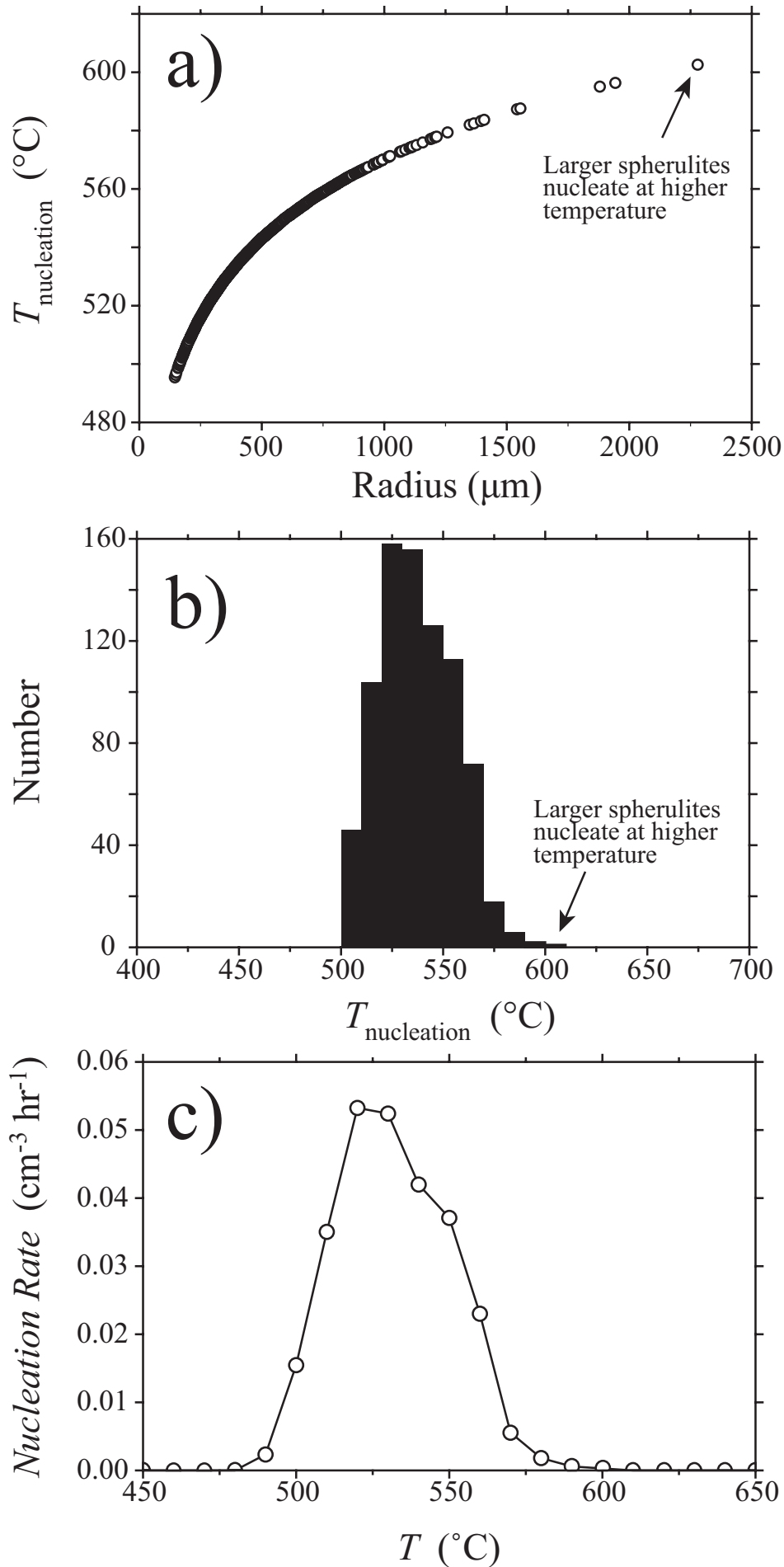
614
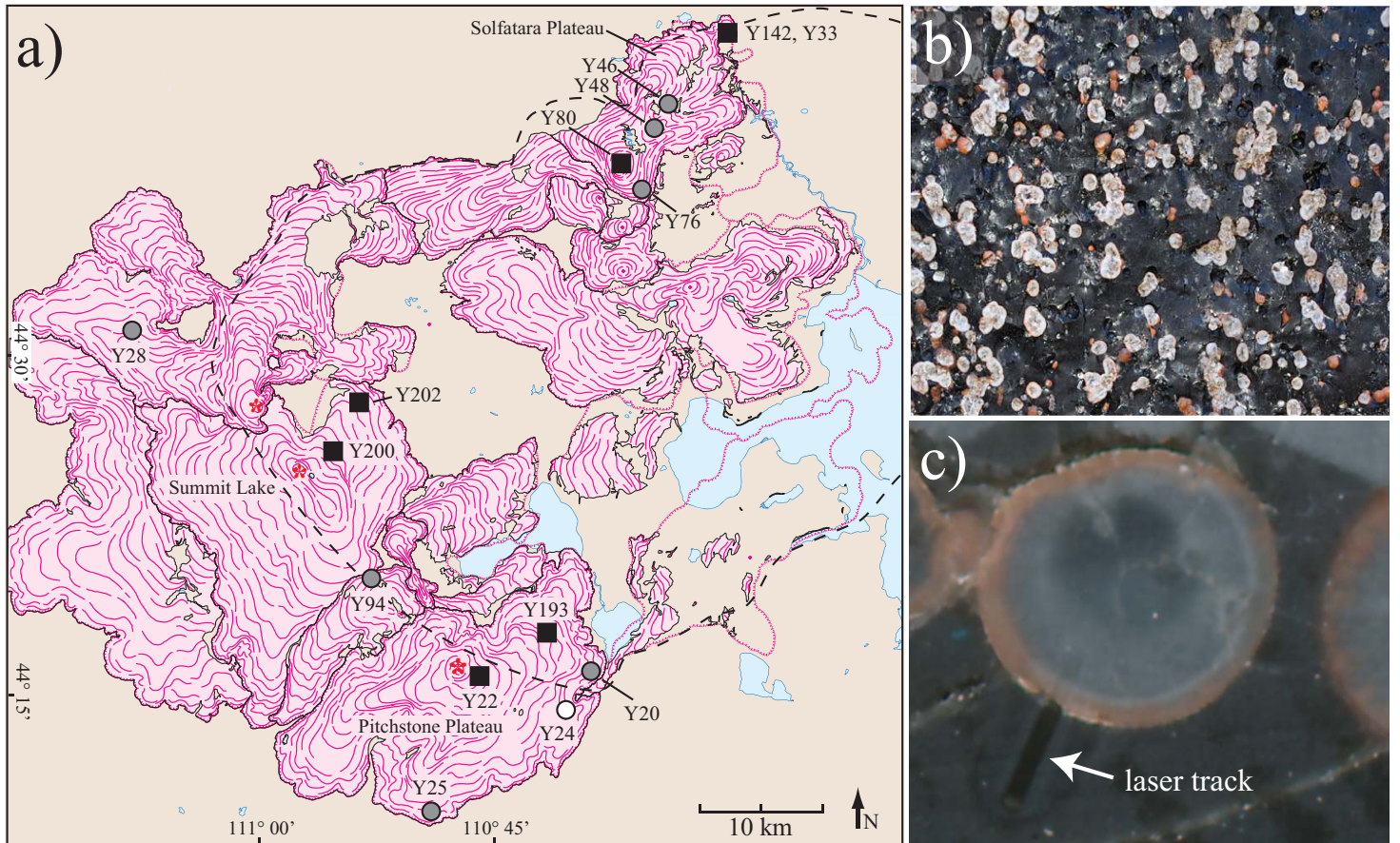
Figure 1
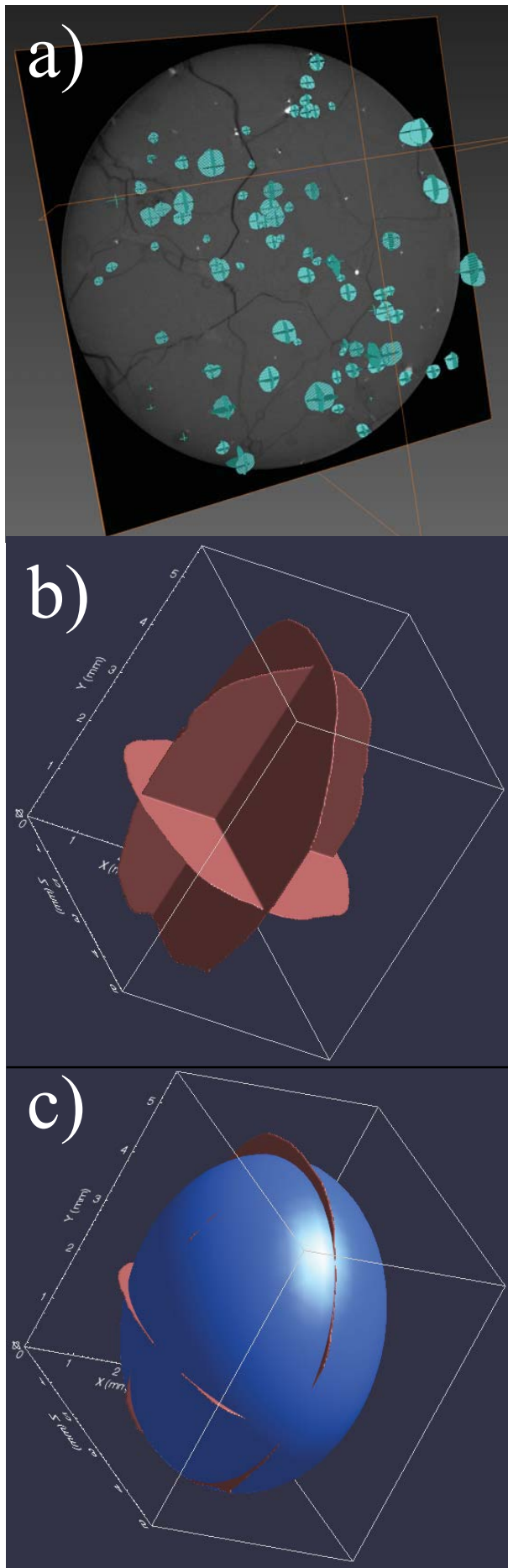
Figure 2
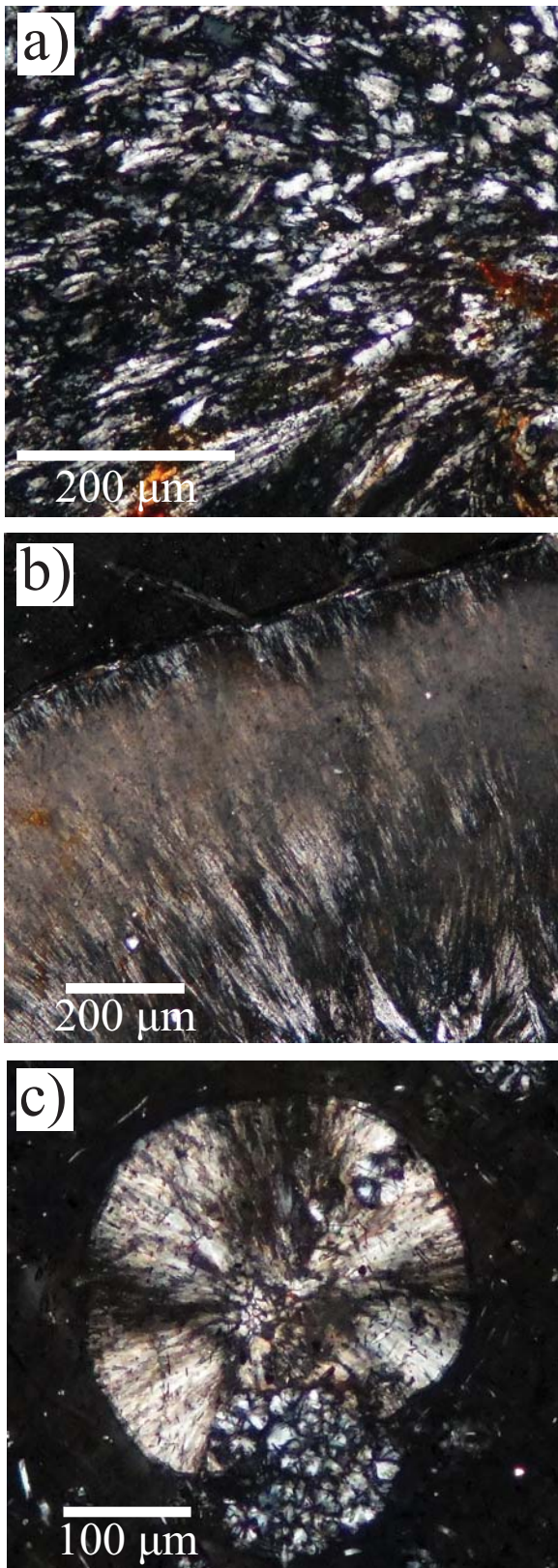
Figure 3
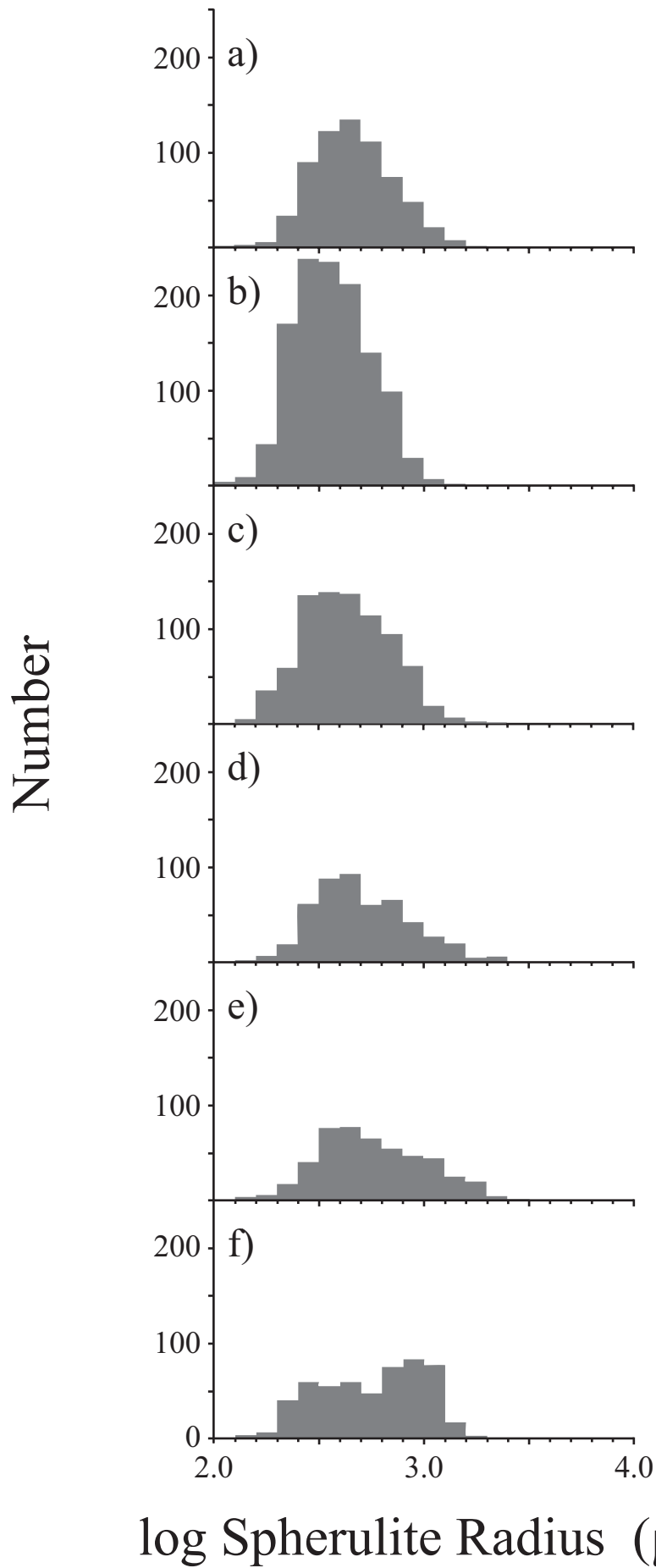
log Spherulite Radius (μm)

Figure 4

Figure 5

Figure 6
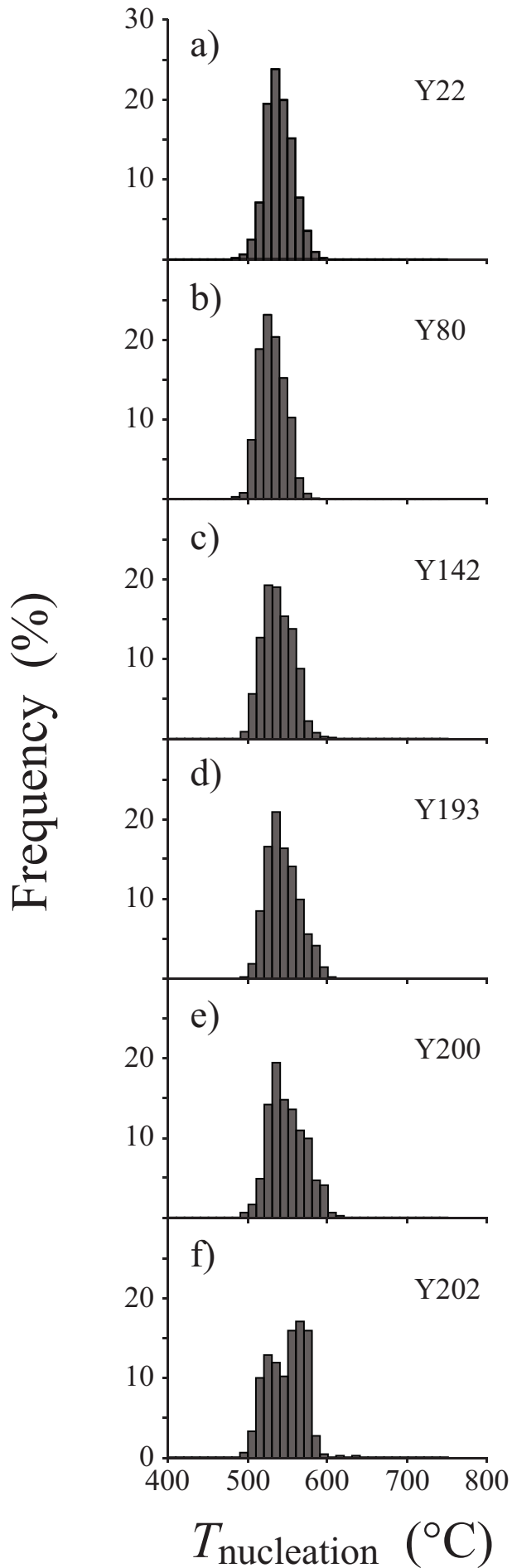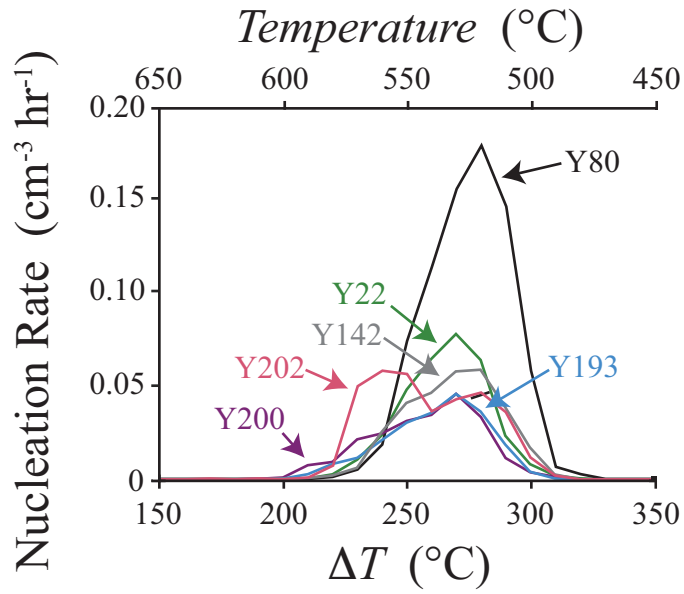
Figure 7

Figure 8

Figure 9